In-Process Machining Distortion Prediction Method Based on Bulk Residual Stresses Estimation from Reduced Layer Removal

Maria Aurrekoetxea [1], Luis Norberto López de Lacalle [2], Oier Zelaieta [1] and Iñigo Llanos [1,*]

1   IDEKO, Basque Research and Technology Alliance (BRTA), Arriaga Industrialdea 2, E-20870 Elgoibar, Spain; ozelaieta@ideko.es (O.Z.)
2   Department of Mechanical Engineering, Bilbao Faculty of Engineering, University of the Basque Country (UPV/EHU), Alameda de Urquijo s/n, E-48013 Bilbao, Spain; norberto.lzlacalle@ehu.eus
*   Correspondence: illanos@ideko.es; Tel.: +34-943-748-000

Abstract: Manufacturing structural monolithic components for the aerospace market often involves machining distortion, which entails high costs and material and energy waste in industry. Despite the development of distortion calculation and avoidance tools, this issue remains unsolved due to the difficulties in accurately and economically measuring the residual stresses of the machining blanks. In the last years, the on-machine layer removal method has shown its potential for industrial implementation, offering the possibility to obtain final components from blanks with measured residual stresses. However, this measuring method requires too long an implementation time to be used in-process as part of the manufacturing chains. In this sense, the objective of this paper is to provide a machining distortion prediction method based on bulk residual stress estimation and hybrid modelling. The bulk residual stresses estimation is performed using reduced layer removal measurements. Considering bulk residual stress data and machining-induced residual stress data, as well as geometry and material data, real-part distortion calculations can be performed. For this, a hybrid model based on the combination of an analytical formulation and finite element modelling is employed, which enables us to perform fast and accurate calculations. With the developments here presented, the machining distortion can be predicted, and its uncertainty range can be calculated, in a simple and fast way. The accuracy and practicality of these developments are evaluated by comparison with the experimental results, showing the capability of the proposed solution in providing distortion predictions with errors lower than 10% in comparison with the experimental results.

Keywords: machining distortion; airframe; residual stress; aluminium

1. Introduction

Machining distortion is a longstanding technical hitch in the manufacturing of structural monolithic components for the aerospace market. A study by the aircraft company Boeing estimated the reworking and scrap cost due to part distortions to be over USD 290 million for four aircraft programs, while revealing that thin-walled aerospace parts stand a 47% chance of having geometrical or dimensional non-conformities after machining [1]. In other sectors, the costs of eliminating component distortion add up to around EUR 850 million in Germany alone, according to the Association of German Mechanical and Plant Engineering (VDMA) [2].

Predicting machining distortion in structural monolithic components is the key to eliminating the costly and long sequential machining processes based on machining layer by layer, turning the part over, and compensating for distortion as it occurs. A great extent of the distortion minimisation and control strategies are based on performing distortion predictions under different machining and clamping strategies and choosing the one leading to minimal distortion according to simulation results. The calculation models used to perform

distortion predictions can be numerical or analytical. While numerical models offer higher accuracy but long computation times [3], analytical models are fast but make assumptions that are too broad to be used in real structural monolithic component geometries [4]. To overcome the limitations of both approaches, hybrid models are developed, which perform fast and accurate distortion predictions and enable future industrial implementation [5].

In order to use distortion prediction models, distortion sources must be acknowledged and quantified. The sources of machining distortion can be grouped into Residual Stresses (RS), machining thermal–mechanical loads (cutting forces and heat), and clamping loads. At the same time, RS can be divided into two categories, namely Bulk or blank Initial Residual Stresses (BIRS) inherited from the upstream manufacturing processes and Machining Induced Residual Stresses (MIRS) as a result of the high-temperature gradients and plastic deformations produced by the cutter on the machined surface. According to the bibliography, BIRS and MIRS are the main distortion sources in the case of structural monolithic components for the aerospace market [6,7]. While BIRS causes distortion when stressed material is taken away, the initial equilibrium is broken and stress relaxation occurs; MIRS on the machined surface cause distortion as they introduce a bending moment into the part [8].

In the specific case of aluminium alloys, the impact of BIRS is considered more significant than the impact of MIRS [9], especially in parts considered thick aeronautical aluminium parts [10,11]. Due to the close link between BIRS magnitude and machining distortion, pioneer investigations on machining distortions tried to minimise them by reducing BIRS [12]. Although BIRS reductions of over an order of magnitude [13], yielding values of ± 30 MPa (which are of the order of the measurement techniques' experimental uncertainties for most of the bulk stress measurement techniques [14]), have been achieved, it is not possible to completely remove BIRS in the machining blanks and guarantee, in this way, distortion-free parts [15]. Thus, the challenge is to manage RS by choosing the optimal machining strategy which minimises distortion. A recurring strategy used to minimise distortion in structural monolithic components chooses the best location of the part within the blank [16,17]. The location choice is based on the distortion simulation results obtained using RS data. However, in reality, distortion simulations may have large errors when compared with experimental results, ranging for simple geometries from 19 to 40% to 50% for complex aerospace parts [18].

In fact, there are two main reasons for these errors. One relies on the over-simplification of the problem leading to models with assumptions that are too wide and which do not represent reality, such as those which ignore systematic BIRS or MIRS [19,20]. The other reason for discrepancies between the simulated and experimental results is linked to the input data used for the simulation, the quantitative assessment of which is challenging and variations inevitable. Indeed, variations in BIRS profiles can occur easily for many reasons, such as the position of a part within the whole batch [21], even when repeating the process in detail [22]. This makes it necessary to characterise BIRS in every blank to ensure the accuracy of distortion calculation models. Another problem related to BIRS characterisation is that most employed measuring methods are destructive and have to be performed in laboratory environments and test samples [23,24]. In this way, recent upgrades of the traditional Layer Removal (LR) method enable measuring BIRS in blanks from which final parts can be obtained [25]. Although the on-machine LR does not require laboratory environments nor special tools to be performed in real parts, its integration as part of a production chain is limited by the long time required for it to be carried out. Finally, it must be noted that distortion research is mainly performed in simple test parts instead of real part geometries, which hinders the integration of the developed models and methods into the industry [6,26].

This paper presents the distortion prediction of an aluminium structural monolithic component using a new approach implementable in industrial environments as part of the production process. The proposed reduced LR tests allows for the agile on-machine identification of the BIRS state of the parts before their machining, while the hybrid distor-

tion model enables fast distortion calculations of the parts, including uncertainties from experimental sources. The results are validated against the experimental results with a good degree of accuracy, showing the capability of the present approach to provide valuable input for the application of distortion minimisation strategies and countermeasures.

2. Materials and Methods

2.1. On-Machine LR in Ribbed Geometries: Semi-Non-Destructive Method

In the on-machine LR method, through-thickness stresses are calculated from deformation measurements which occur after removing subsequent layers of the material of the machining blanks. The on-machine LR method iterates the machining and measurement steps between which the part is clamped and released in order to allow the deformation resulting from the stress relaxation. From the deformation data measured by machine-integrated probing (p), a curvature progression is obtained (χ). Although the formulation of the original method is based on the plate bending theory [27,28], its recent upgrades consider the initial curvature of the blanks (χ_0) and the MIRS [29]. Also, it can tackle ribbed geometries when combined with FEM using the equivalent bending stiffness (I^{eq}) approach [25]. The assumptions of the method are small deformations, isotropic homogeneous material in the linear elastic regime, and negligible stresses in the depth direction (Z). Moreover, the main uncertainty source for the on-machine LR method for BIRS characterisation is the on-machine probing measurements, which were analyzed in a previous work [30]. Therein, the effect of these uncertainties on the stress measurements and consequent curvature calculations was analyzed, and different methods of minimizing such effects were evaluated. It was observed that the uncertainties on the final curvature calculations can be significantly reduced by convoluting the curvature measurements with a weighting function of triangular shape and cut-off [30]. Nevertheless, completely removing the uncertainty is not feasible, and the uncertainty of the BIRS input data affects the distortion simulation results, which are also bounded by uncertainty bands. The uncertainty of the BIRS data can be estimated through Monte Carlo simulations, introducing random probing errors into the measured curvatures [30].

Although the on-machine LR method enables obtaining the actual stresses of a machining blank and manufacturing the part from the same blank, performing a complete LR test involves iterative clamping, machining, and measuring phases which are very time-consuming and hinder the use of the method as part of the manufacturing chain.

2.2. Reduced LR Measurement and BIRS Estimation

In order to avoid a complete LR test, the proposed reduced LR is based on performing only 5 LR steps on the blank and then estimating the BIRS profile through a comparison of the results with a full LR in a whole blank (all LR steps). In this way, the reduced LR, consisting of 5 layers, does not require a long time to be performed and thus has a higher potential to be implemented in production lines.

With the curvatures of the full LR performed in an analogous blank and the curvatures of the ribbed and reduced LR, the concept of BIRS estimation assumes that, although BIRS vary from one blank to another, blanks of the same characteristics have the same stress profile shape. Figure 1 illustrates this point, showing BIRS profiles for three different blanks, B1, B2, and B3, with different stress values but an analogous through-thickness shape.

In this way, the procedure of reduced LR and BIRS estimation consists of the following steps, which are depicted in Figure 2.

1. Perform a BIRS measurement in one blank ($B1$) by on-machine full LR. In this way, the through-thickness stress profile (σ_{B1}) of a blank of the same characteristics (material, geometry, supplier, and batch) as the one that will be used for manufacturing the final part ($B2$) are obtained.
2. Plan the machining strategy of the final part, including 5 layers of machining, full roughing, and finishing phases. These layers can be machined with ribs if the final

part geometry requires it. As a minimum, an approximate depth of 15% of the height is considered to provide good results in terms of accuracy.

3. Perform the ribbed reduced LR of 5 layers in the blank from which the final part will be manufactured (*B2*) and measure the associated curvatures χ_{B2}^{exp}).

4. Calculate the curvatures χ_{B2}^{sim} with the inverse LR formulation, using as input data the BIRS measured in the blank *B1* (σ_{B1}), the layer discretisation and geometry (ribs layout) of *B2*, and the equivalent bending stiffness I_{B2}^{eq}.

5. Determine the BIRS estimation coefficient c_x using Equations (1) and (2) (with analogous expressions applying to Y direction), *m* being the number of LR steps performed, i.e., 5 LR steps, and *ν* being the Poisson's ratio.

$$c_{x,i} = \frac{\left(\chi_{B2,x}^{exp}\right)_i + \nu\cdot\left(\chi_{B2,y}^{exp}\right)_i}{\left(\chi_{B2,x}^{sim}\right)_i + \nu\cdot\left(\chi_{B2,y}^{sim}\right)_i} \tag{1}$$
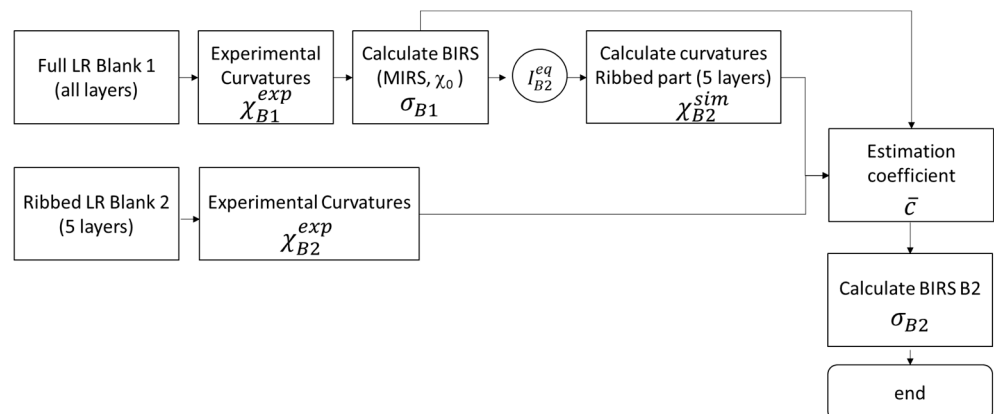
$$c_x = \frac{\sum c_{x,i}}{m} \tag{2}$$

6. Obtain the estimated BIRS corresponding to blank *B2* ($\sigma_{B2,x}$) using Equation (3).

$$\sigma_{B2,x} = c_x\cdot\sigma_{B1,x} \tag{3}$$
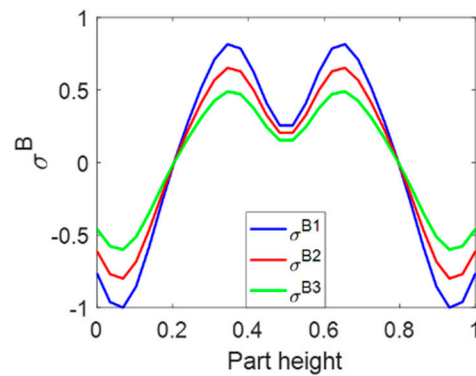
Figure 1. Normalised BIRS profiles in different blanks fulfilling the hypothesis of different stress values with the same profile shape.

Figure 2. Procedure of reduced LR and BIRS estimation.

For the case of long parts where the distortion is predominantly generated in one spatial direction, the formulation shown above can be simplified to 1D by applying the same equations but setting the Poisson's ratio (*ν*) to zero value.

2.3. Distortion Prediction and Uncertainty Assessment

The hybrid distortion prediction model consists of combining the agility of the analytical modelling and the better accuracy of numerical modelling for assessing geometries with ribs typical of structural monolithic components. Figure 3 schematically shows the flowchart for the hybrid distortion prediction considering BIRS and MIRS as the input load data, where the numerical part only needs to be run once in a setting-up phase. The model is built using the commercial software Matlab R2022a.
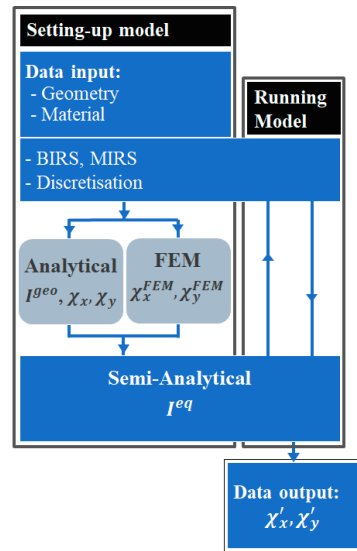

Figure 3. Hybrid distortion model flowchart.

The analytical model is based on the bending moment theory and thus uses the analogous but inverse formulation of the on-machine LR [25,30], meaning that this one calculates the curvature considering the material of the part instead of the removed material. Figure 4 shows a schematic cross section for the analytical model, where the target geometry is discretised in layers where e_i is the layer thickness, w_i is the material left in each layer, and k_{ij} is the leverage or distance between the neutral plane of each layer i and the neutral plane of the whole part at a specific machining step j. The MIRS and BIRS profiles are shown as solid green and blue lines respectively. The solid red line represents the stresses due to initial curvature bending and, finally, the solid black line is the summation of the original BIRS (blue) and initial curvature (red) stresses.
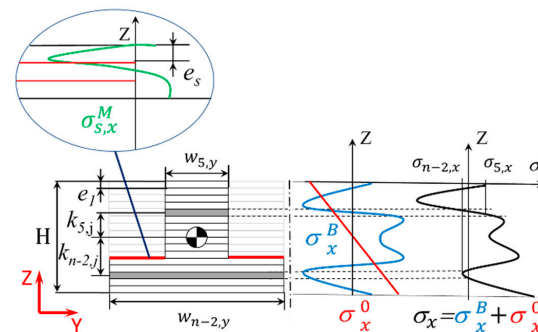

Figure 4. Discretisation of a final part section for the analytical distortion model, including input stresses.

Equations (4)–(6) show the mathematical relations from which the curvature in the X direction is obtained, where E is the Young's modulus of the material, Mb_x and Mb_y are the bending moments in the X and Y directions, and I_x and I_y are the second moments of

the area. $\sigma_{i,x}^{B}$, $\sigma_{i,x}^{M}$, and $\sigma_{i,x}^{0}$ correspond to the BIRS, MIRS, and the stresses due to the initial part curvature, all in the X direction.

$$\chi_x = \left(\frac{Mb_x}{E \cdot I_x} - v \cdot \frac{Mb_y}{E \cdot I_y} \right) + \left(\frac{Mb_x^{M}}{E \cdot I_x} - v \cdot \frac{Mb_y^{M}}{E \cdot I_y} \right) \tag{4}$$

$$Mb_x = \sum_{i=1}^{n} \left(\left(\sigma_{i,x}^{B} + \sigma_{i,x}^{0} \right) \cdot e_i \cdot w_i \cdot k_{ij} \right) \tag{5}$$

$$Mb_x^{M} = \sum \left(\sigma_{i,x}^{M} \cdot e_s \cdot w_i \cdot k_{ij}^{s} \right) \tag{6}$$

Analogous expressions apply to the X-Z cross-section and Y direction. Again, in parts with long shapes, for which a 1D formulation is enough to capture the main distortion in the longitudinal direction, Equation (4) can be used in 1D by setting the Poisson's ratio to zero.

In the numerical model performed with the ANSYS 2021 R1 software [31], the geometry is meshed in specific heights in the Z direction, so that RS (namely, BIRS and MIRS) can be input in Command Snippets through the command Inistate according to node locations in the model. The element type selected for the model is Solid 186 (second-order 20 node hexahedrons) [31] and the element size varies from 0.01 to 1 mm depending on the part zone and the need to introduce the initial stress states. The boundary conditions employed were remote displacement with deformable behavior [31], avoiding rigid body motions on the part while enabling free deformations on it. Both the effect from element size and from boundary conditions were evaluated by performing several tests with simplified and actual part geometry until obtaining a convergent model behavior with adequate computational time (less than 5 min).

The two models are merged so that the equivalent bending stiffness (I^{eq}) is obtained and input into the analytical formulation, becoming the hybrid distortion model.

Apart from the model, to perform the distortion prediction, the BIRS of the blank B2 (σ_{B2}), as well as the MIRS measured in the machined surfaces, the initial curvature of the blank (χ_0), and the equivalent bending stiffness (I^{eq}), are needed as input data. An important part of distortion prediction consists of determining its uncertainty. A substantial portion of this distortion prediction uncertainty can be obtained considering the BIRS measurement inaccuracies, the main source of which are probing errors [30]. The workflow used to calculate this confidence range is depicted in Figure 5 where only probing errors are introduced as uncertainty sources of the BIRS measurement.

In this way, starting with the BIRS profiles measured by on-machine full LR in blank B1 (σ_{B1}^{exp}), and using the procedure previously described, a cloud of BIRS profiles with probing error (σ_{B1}^{MC}) is obtained, which corresponds to 2000 iterations.

After this, the cloud of BIRS profiles with probing error is used for calculating the curvatures, but this time with the layer discretisation and width of the blank $B2$. As $B2$ is the blank from which the final part is obtained, if the LR is ribbed, the equivalent stiffness (I_{B2}^{eq}) is required for obtaining the cloud of curvatures (χ_{B2}^{MC}) in this step.

Relating this cloud of simulation curvatures with the experimental curvatures measured in the reduced LR of $B2$ (χ_{B2}^{exp}) using Equation (1), a cloud of estimation coefficients (c^{MC}) can be obtained. With these coefficients and Equation (3), the cloud of BIRS of $B2$ (σ_{B2}^{MC}) is calculated. From this cloud of stresses, the BIRS estimation uncertainty linked to probing errors is obtained.

Finally, the distortion of the final component ($\chi_{B2,F}^{MC}$) is calculated using the estimated BIRS, the equivalent bending stiffness of the final part ($I_{B2,F}^{eq}$), and the MIRS and clamping stresses linked to the measured initial curvature of the blank. As the estimated BIRS are not a single profile, but a cloud of them representing the measuring uncertainty of the LR, the hybrid distortion model (based on the analytical inverse LR formulation and equivalent bending stiffness), is used for the distortion calculation. The distortion output is then a

cloud of final distortion values from which the uncertainty of the distortion simulation can be calculated for a confidence level of 99.7% (3σ).
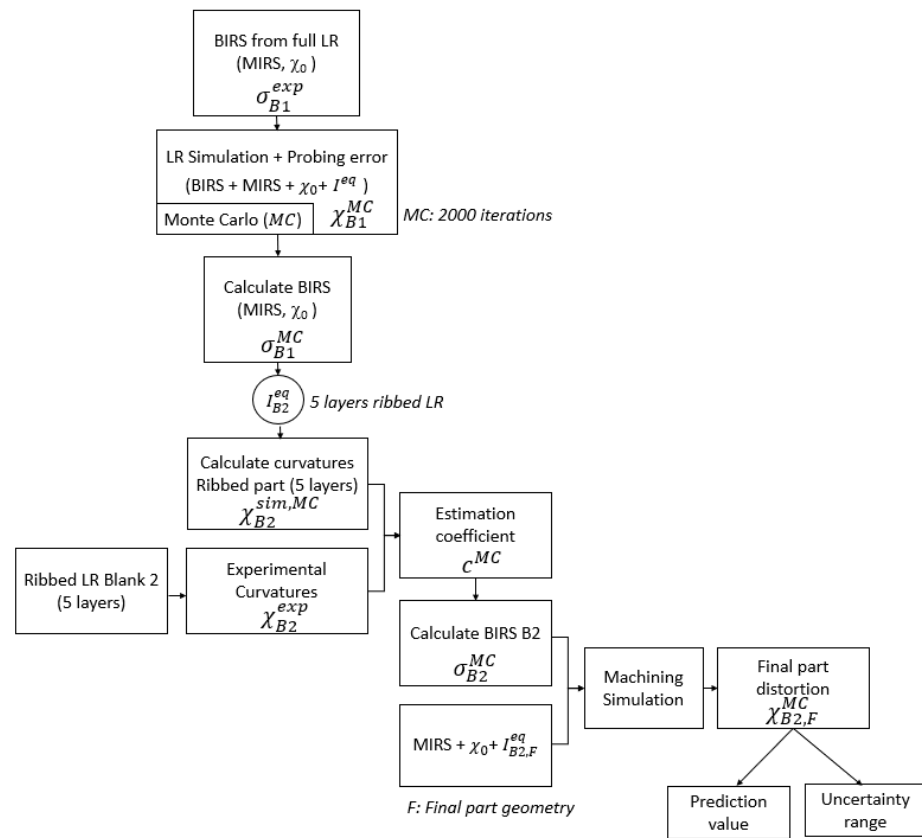
Figure 5. Procedure for final part distortion prediction, including uncertainty.

2.4. Test-Case Definition and Experimental Procedure

The proposed methodology was applied to Al7175−T3451 parts for experimental verification. The mechanical properties of this alloy are displayed in Table 1.

Table 1. Mechanical properties of Al7175−T7351.

Material	Density (g/dm^3)	Hardness (HRb)	Young Modulus (GPa)	Poisson's Ratio (-)
Al7175-T7351	2.8	135	71.7	0.33

The part geometry represented a simplification of a real structural monolithic component provided by an aerostructure manufacturer. Therefore, the simplified part geometry contained the key features (dimensions in mm, ribs layout, walls, and floor thickness) of the real part (Figure 6a), whose dimensions are defined in Figure 6b.

In this component, the aerostructures manufacturer reported recurring non-conformities due to machining distortion (approximately 50% of the parts showed significant distortions), the flatness tolerance being 0.3 mm (Figure 7).

(a)   **(b)**
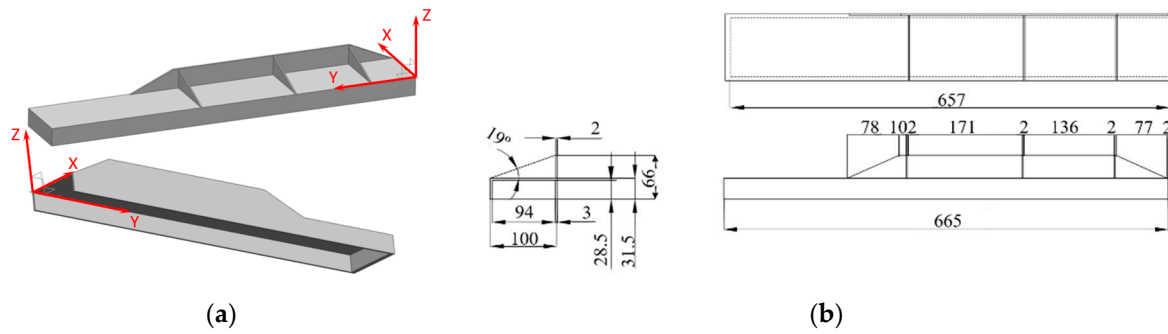
Figure 6. (**a**) Al7175-T7351 part geometry for the machining distortion analysis; (**b**) Dimensions of the part in millimeters.
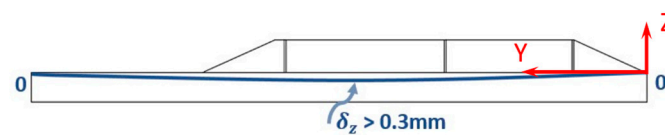
**Figure 7.** Recurring distortion shape and amplitude in the machining of the Al7175-T7351 component.

The component had ribs on both sides of the floor with different heights and shapes. The ribs of the lower side of the part formed a U-shape or a pocket with one of the short sides open and had a 3 mm thickness. The upper side of the part had three triangular ribs in the transverse direction, and one in the longitudinal direction, all having a thickness of 2 mm; none of them were centered. In order to perform the reduced LR, first, the part side in which these measurements were taken was chosen. Due to the test-case geometry, we decided to carry out the LR on the side where the fins have an open pocket shape.

The dimensions of the machining blanks used in the study for machining were $130 \times 700 \times 80$ mm. Three blanks were used, one for the full LR and BIRS characterisation and the other two for the experimental verification of the distortion model, meaning that final parts were obtained from them after estimating the corresponding BIRS in each blank. All blanks left an offset of 14 mm for locating the part in different positions. In this way, each of the two final parts was located at one specific offset position, as depicted in Figure 8. While Part a was located at the lowest position, machining just 1 mm from the pocket side for cleaning purposes, Part b was centered in the blank, leaving 7 mm at each side.
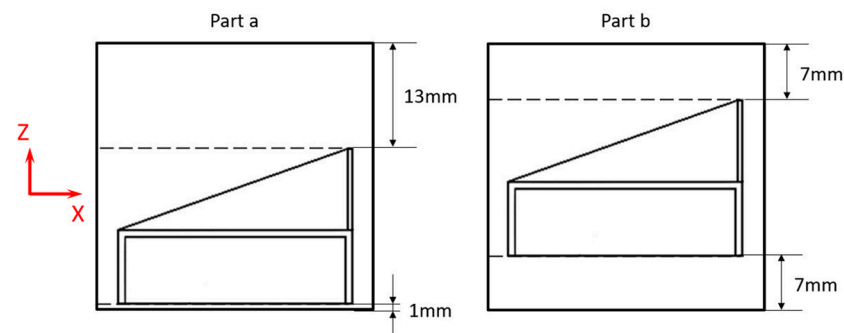
Figure 8. Part location within the blank and offset in each of the sides.

Concerning the RS input data for the distortion model, as mentioned, BIRS were estimated using the procedure described in Section 2.2 (including reduced LR), and MIRS were measured by incremental hole drilling. Figure 9 shows the measuring locations in the two parallel machined surfaces (pocket side and ribbed side).
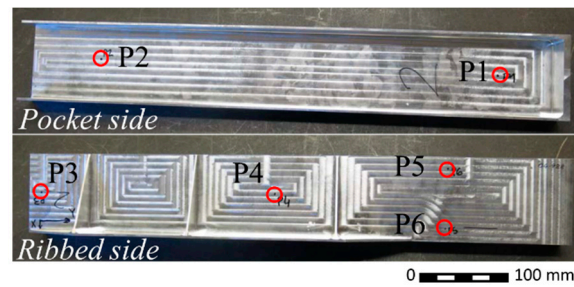
Figure 9. MIRS measuring locations in the Al 7175-T7351 machined part.

Considering the part dimensions and the high height-to-width ratio (>0.6), the 1D formulation was used.

The machining operations were also carried out on a Soraluce FMT 4000 multitasking machine. For the test, two milling tools were used, a face mill D80mm Kennametal 80A05RP90BG15C1WPM with 5 inserts BGHX15L5PCFRGG-K110M for the LR and the roughing operations, and an end-mill D16 mm Ceratizit W.H-SA.16,0.45.Z3.R1,0.HA.K TI1005 with 3 cutting edges for finishing operations. For the on-machine probing of the LR, a Renishaw RMP600 high-accuracy touch probe was used.

A four-setup machining strategy was chosen to reach all the faces of the part. Figure 10 depicts all the setups of the CAM simulations taken from the Nx software. The first setup, depicted in Figure 10a, corresponds to the reduced LR, including layer machining (Figure 11a) and probing (Figure 11b). In this setup, the pocket-side machining was also carried out, including roughing and finishing operations. Then, the part was turned over and the side of the triangular ribs was machined (roughing and finishing), as shown in Figure 10b. Finally, the lateral sides of the part (Figure 10c,d), which had an offset of 1 mm each, were machined in setups 3 and 4.
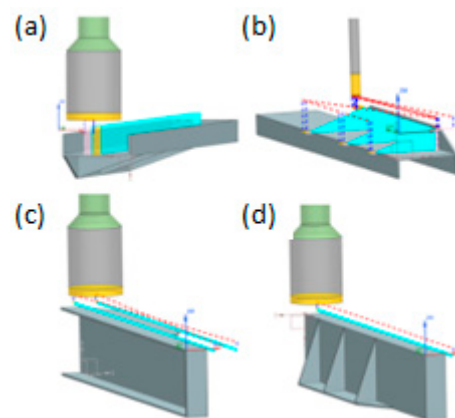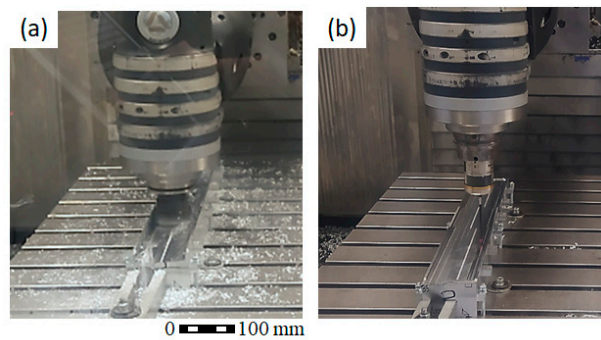

Figure 10. (**a**) Setup 1: open pocket side machining; (**b**) Setup 2: triangle-ribbed side machining; (**c**) Setup 3: small lateral side machining; (**d**) Setup 4: large lateral side machining.

The machining conditions for the two tools are defined in Table 2, being 4000 rpm or the maximum spindle speed available. The axial and radial depth of the cut varied for each operation. Figure 12 depicts the actual machining operations of Parts a and b in setups 1 and 2, respectively. The parts were clamped with bolts and T-nuts to the machining table.

Table 2. Machining conditions used for the experimental test.

| Parameter	D80 mm	D16 mm
Spindle speed—n (rpm)	1800	4000

Figure 11. Reduced on-machine LR in Setup 1, open pocket side: (**a**) machining of a layer j; (**b**) probing.
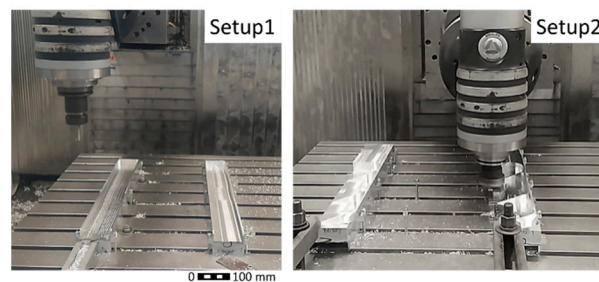
Figure 12. Machining of the two Parts a and b in Setup 1, open pocket side, and Setup 2, triangle-ribbed side.

Regarding the measurements, while the probing for the LR was performed in the machine with a touch-probe in a grid of 3×9 points (Figure 11b), due to the low stiffness of the final part (Figure 13a) and the corresponding swinging and elastic deflections caused by the machine-integrated touch-probe, the final part measurements were obtained by contact scanning in a CMM Zeiss PRISMO 9/15/7 (Figure 13b) with a measurement uncertainty bellow 1 μm using a 10 mm/s scanning speed. The scanning was performed gathering data every 1.5 mm on 10 transversal lines on the part, with each line distanced 70 mm in the longitudinal direction from the part.
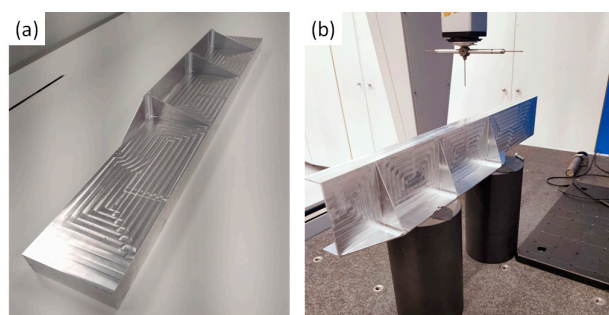

Figure 13. (**a**) Final part machined; (**b**) Measurements in a CMM.

3. Results

3.1. Input Data for the Distortion Prediction

BIRS in the part longitudinal (Y) direction were obtained using the concept of reduced LR and BIRS estimation previously introduced in Section 2.2. Therefore, the first step entailed performing a BIRS measurement by full on-machine LR in one blank, labelled for now on as σ_{full}^{B}, including the uncertainty due to probing errors in a range of 0.010 mm [30], which is depicted in Figure 14 with red bars.
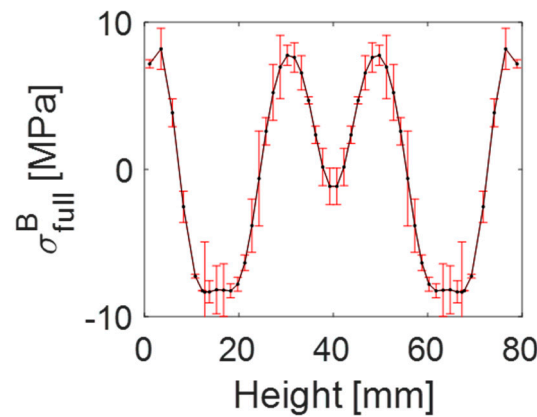
Figure 14. BIRS in the part longitudinal (Y) direction measured in a machining Al7175−T7351 blank of 130 × 700 × 80 mm by on-machine Full LR.

The results show that the obtained BIRS had low magnitude and an M-shape profile, different from bibliography data on the same material, which showed a bell-shape profile measured by the contour method [32]. This discrepancy could be related to the different thicknesses on the test parts in both studies [14]; the thickness was 80 mm in this study while in [32] it was 36 mm.

Next, the BIRS in the two parts (a and b) were estimated following the procedure described in Section 2.2. Reduced LR was performed in two blanks of the same batch, material, and dimensions. Figure 15 shows the experimental curvatures measured in the reduced LR of the two blanks with dotted lines, and the simulation values of ribbed LR with lines with crosses. These simulation results were calculated with the inverse LR formulation (Equations (4)–(6)) [25], and, as input data, the BIRS measured in the blank by full LR σ_{full}^{B}, the MIRS measured in the machined surfaces, the initial curvature (χ_0), the geometry discretisation and rib layout, and the equivalent bending stiffness I^{eq}.
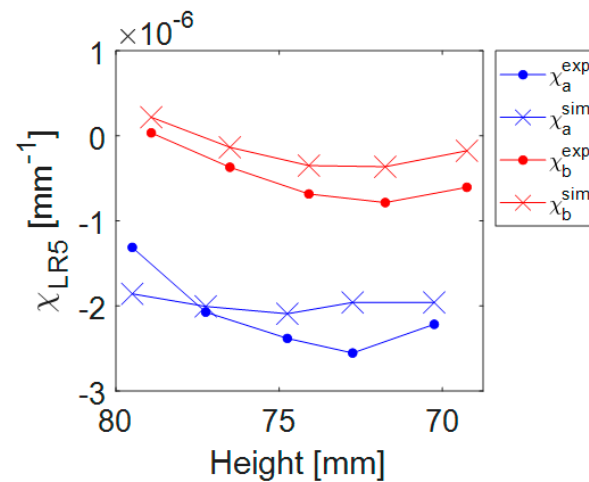

Figure 15. Curvature (χ_{LR5}) data obtained from the reduced LR method for both experiments and simulations performed with the BIRS in Figure 14.

As can be seen, while, in the blank of Part a, the two curvature progressions crossed each other, in the blank of part b they were parallel. Moreover, while, on one of the blanks, all curvatures were near zero, in the other one they had higher absolute values. Both events were linked mainly to the initial curvature combined with the high stiffness of the part during the removal of the first five layers.

With these values, the BIRS estimation coefficients were obtained with Equations (1) and (2). The resulting BIRS profiles in the part's longitudinal (Y)

direction for the two blanks were calculated using Equation (3) and are displayed in Figure 16. The results show that, while the stress magnitude in blank a was slightly bigger than the base BIRS of the full LR (σ^B_{full}), in blank b the BIRS magnitude approximately doubled those values.
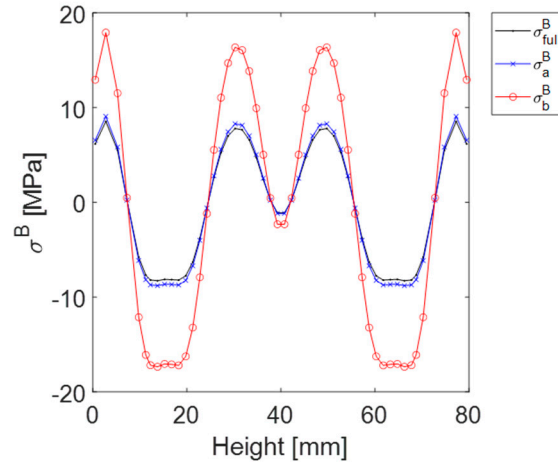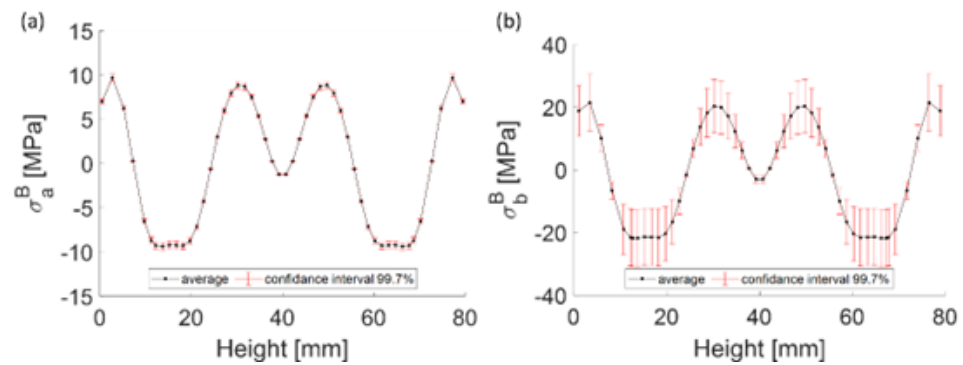

Figure 16. BIRS in the part longitudinal (Y) direction obtained by full LR in one sacrificial blank (σ^B_{full}) and estimated BIRS for the blanks a (σ^B_a) and b (σ^B_b), from which final parts were obtained.

Once the final parts were machined, the induced stresses were measured on the surfaces (Figure 9) by incremental hole drilling [33,34]. The MIRS profiles (σ^M) obtained in the part's longitudinal (y) direction (1D formulation used due to the high height-to-width ratio) are depicted in Figure 17a. The error bars at each measuring point correspond to the incremental hole drilling measurement uncertainty calculation according to [34]. As can be seen, compressive shallow (0.05 mm penetration depth) MIRS were induced using these machining conditions, where the highest uncertainty was near the surface and, for some of the points, was above the stress value. Averaging the MIRS of the six locations, Figure 17b shows the MIRS, where the error bars represent the variability of stresses linked to the measurement location (standard deviation) at each depth. Compressive shallow (0.05 mm penetration depth) MIRS were induced, with the maximum amplitude of stresses being approximately −30 MPa. The variability observed is in accordance with similar measurements in the Al7050-T7451 alloy shown in [35] and performed both by hole-drilling and XRD techniques.
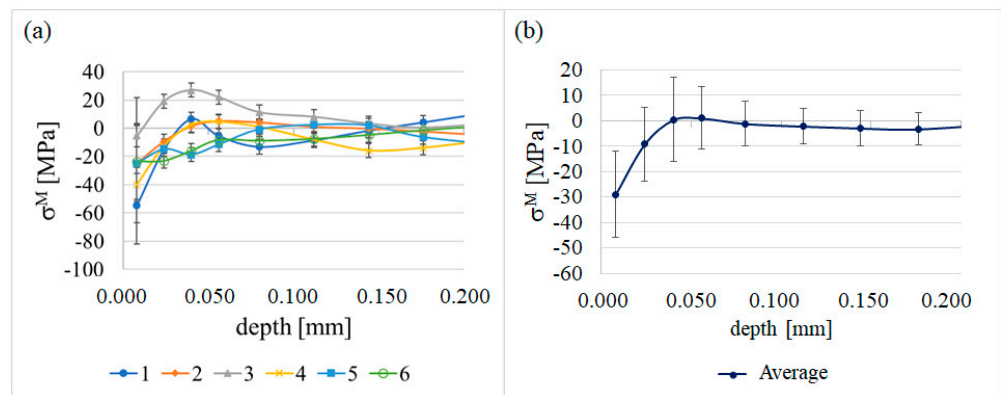
Figure 17. MIRS in the part's longitudinal (Y) direction measured in the Al7175-T7351 final part by incremental hole drilling: (**a**) at different locations with the error bars representing the tabulated uncertainty of the method; (**b**) average MIRS of all points with the error bars representing the variability (standard deviation) between points.

Following the workflow of Figure 5, the BIRS in the part's longitudinal (Y) direction with probing uncertainty for each of the parts were obtained, as Figure 18 shows. The uncertainty of the BIRS of Part b was much higher than the uncertainty of Part a. This was because the curvature values of Part b were near zero (Figure 15), so the part deflections (δ_z) were close to the probing uncertainty used as input data (0.01 mm).

Figure 18. BIRS estimated in the part's longitudinal (Y) direction with uncertainty ranges including measuring uncertainty due to probing errors: (**a**) Part *a*; (**b**) Part *b*.

3.2. Distortion and Uncertainty Results

To obtain the equivalent bending stiffness of the final part, the numerical part of the hybrid model was run [25]. Figure 19 shows the FEM directional deformation in the Z axis results obtained for Parts a and b using the estimated BIRS (Figure 16), MIRS (Figure 17b), the initial curvature, and the final part geometry as input.
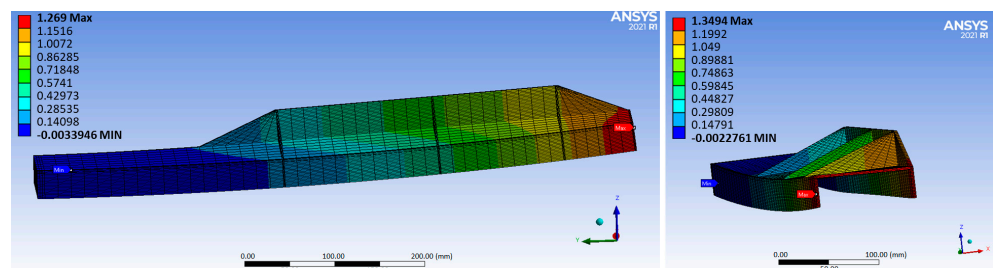
Figure 19. Distortion FEM simulation for obtaining the final part equivalent bending stiffness of Parts a and b, displayed in two different orientations.

For the uncertainty of the distortion prediction, the hybrid model was run iteratively for all BIRS profiles previously calculated, obtaining a cloud of final part distortions from which the uncertainty of the distortion prediction was calculated.

Finally, the distortion simulation results were contrasted with the experimental results for both parts. For these experimental results, two different measurements were taken in the final parts, one in a grid equal to the on-machine probing for the LR (Figure 20a) and another one sweeping the surface in the pocket side (Figure 20b). Together with the measurement values, the surfaces corresponding to the second-order regressions of those measurements employed for the calculation of the part's curvature values [28] are shown.

The final comparison of the simulated and experimental distortion results is depicted in Figure 21, where the maximum deformations in the Z direction of the part are plotted. The black hollow circles are the experimental results, the red dots are the simulation results, and the red bars represent their uncertainty range. These results are also gathered in Table 3, where experimental deformations (δ_z^{exp}), simulation deformations (δ_z^{sim}), the difference amongst them (error), and the simulation uncertainty range are gathered for the test-part length (665 mm).
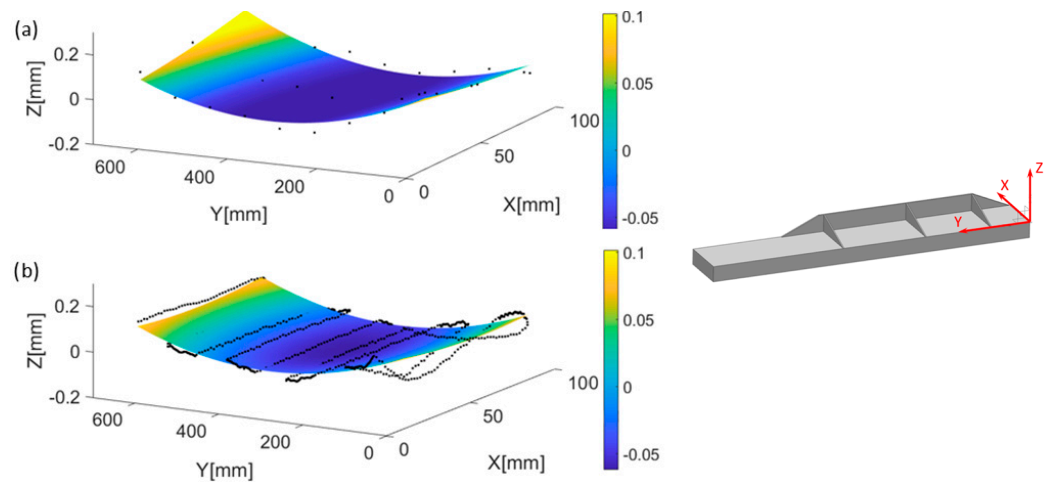
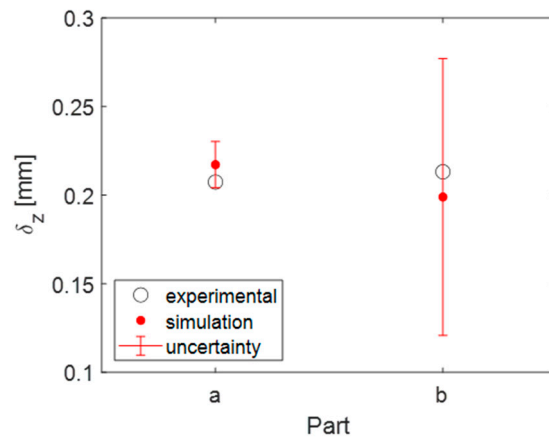**Figure 20.** Final part probing in Part a: (**a**) grid 3 × 9; (**b**) sweeping the open pocket side.

Figure 21. Comparison of deformation in the Z direction of the part obtained from simulation using estimated BIRS, including uncertainty range and experimental values for the two test parts: Part a, Lowest offset; Part b, same offset in both upper and lower sides.

Table 3. Distortion results as deformations in Z direction of the part (δ_z) of the Parts a and b.

Part	δ_z^{exp} (mm)	δ_z^{sim} (mm)	Error (mm)	Error %	Uncertainty (mm)	Uncertainty %
a	0.255	0.273	0.018	7	0.018	7
b	0.262	0.270	0.008	3	0.175	67

4. Discussion

This paper presents a reduced LR and BIRS estimation procedure, and a hybrid distortion prediction which is evaluated through an experimental test of real aerostructure parts.

As can be seen in Figure 21, the difference between the experimental and simulated results was 7% and 3% for Parts a and b, respectively. This demonstrated that accurate distortion predictions can be performed using actual BIRS data obtained from reduced LR and BIRS estimations, as well as measured MIRS, initial curvatures, and equivalent bending stiffness.

Regardless of the different magnitude of BIRS obtained through the estimation, which is approximately double for Part b with respect to Part a (Figure 16), the difference in the experimental distortions was minimal in the two parts—0.010 mm—which was in the range of the probing uncertainty. This was because the offset location had an impact

on the distortion. In this way, for the hypothetical case of blanks with the same BIRS, locating the part centered in the blank would have reduced the distortion for this particular geometry with ribs at both sides of the floor. However, as the results show, the hypothesis of considering equal BIRS in blanks of the same batch, material, and size is inaccurate and can lead to large distortion prediction errors.

Moreover, the experimental results fell within the calculated uncertainty ranges in both cases. This simulation uncertainty was low compared with the experimental distortion value for Part a (7%) while, for Part b, it was very large (67%). It must be noted that a large distortion prediction uncertainty limits the prediction capability of the simulation results to a certain extent. This large uncertainty was linked to the BIRS estimation (Figure 16), which was very sensitive to curvature values near zero because of the coefficients for BIRS estimation. Thus, if the LR curvature progressions are near zero, these are more likely to have higher uncertainty ranges. The curvatures are near zero when the equivalent bending stiffness is high, meaning that the H is large or the rib amount and thickness are large; the curvatures are also near zero when the part dimensions are too small to be able to measure deformations δ_z by probing.

In summary, in this paper, a real-part distortion calculation using estimated BIRS from reduced LR was performed. Bulk residual stresses, machining distortion predictions, and uncertainty ranges were obtained in a simple and fast way. The experimental results demonstrated the prediction capability of the proposed method based on estimating the actual BIRS in the blanks from which the final parts were obtained.

5. Conclusions

This work performs real-part distortion calculations, for which, apart from measured MIRS, a concept of reduced LR and BIRS estimation was presented. This novel concept enabled the easier implementation of machining distortion control strategies in production lines for requiring shorter times to perform BIRS characterisations. In addition, considering the magnitude of the RS measurements obtained within this work, in aluminium, greater attention must be paid to BIRS, as these are the main distortion drivers. In any case, considering their variability, both BIRS and MIRS should be used as input in distortion prediction models to reduce inaccuracies.

From the results of this work, the following general conclusions can be drawn:

1. The hybrid distortion model is an agile and accurate tool for machining distortion calculation, which can be used in different ribbed geometries typical of aerostructures, and enables the performing of distortion analysis at the process planning stage. The model is validated experimentally in aluminium test parts, showing a prediction accuracy, in comparison to experimental results, below 10%, within the uncertainty range calculated. This uncertainty range is linked to the BIRS measurement uncertainty (probing uncertainty of on-machine LR).
2. Considering that performing a complete BIRS measurement is not industrially feasible, the reduced LR and BIRS estimation offers the possibility of obtaining the actual BIRS of the blanks in a cost-effective way, and calculating the machining distortion of final parts, as well as their uncertainty ranges. The experimental results in aluminium aerostructures demonstrate the validity of the approach, which provides an alternative to confronting distortion in production lines.
3. Due to the uncertainty of bulk residual stress measurements, which are the input of the hybrid distortion model, providing a distortion prediction uncertainty range is as important as the prediction itself. In fact, the part geometry and its bending stiffness are factors from which it can be foreseen whether the distortion prediction procedure introduced here is valid or not.

Author Contributions: Conceptualization, M.A., O.Z., L.N.L.d.L. and I.L.; methodology, M.A. and I.L.; software, M.A.; validation, M.A. and I.L.; formal analysis, M.A. and I.L.; investigation, M.A.; resources, I.L and O.Z.; data curation, M.A.; writing—original draft preparation, M.A.; writing—

References

1. Bowden, D.M.; Halley, J.E. *Aluminium Reliability Improvement Program Final Report 60606*; The Boeing Company: Chicago, IL, USA, 2001.
2. Zoch, H.-W. From Single Production Step to Entire Process Chain—The Global Approach of Distortion Engineering. *Mater. Werkst.* **2006**, *37*, 6–10. [CrossRef]
3. Ma, K.; Goetz, R.; Srivatsa, S.K. Modeling of Residual Stress and Machining Distortion in Aerospace Components. *ASM Handb.* **2010**, *22B*, 386–407. [CrossRef]
4. Gao, H.; Zhang, Y.; Wu, Q.; Song, J. An analytical model for predicting the machining deformation of a plate blank considers biaxial initial residual stresses. *Int. J. Adv. Manuf. Technol.* **2017**, *93*, 1473–1486. [CrossRef]
5. Li, B.; Deng, H.; Hui, D.; Hu, Z.; Zhang, W. A semi-analytical model for predicting the machining deformation of thin-walled parts considering machining-induced and blank initial residual stress. *Int. J. Adv. Manuf. Technol.* **2020**, *110*, 139–161. [CrossRef]
6. Akhtar, W.; Lazoglu, I.; Liang, S.Y. Prediction and control of residual stress-based distortions in the machining of aerospace parts: A review. *J. Manuf. Process* **2022**, *76*, 106–122. [CrossRef]
7. Mathews, R.; Sunny, S.; Malik, A.; Halley, J. Coupling between inherent and machining-induced residual stresses in aluminum components. *Int. J. Mech. Sci.* **2022**, *213*, 106865. [CrossRef]
8. Brinksmeier, E.; Cammett, J.T.; König, W.; Leskovar, P.; Peters, J.; Tönshoff, H.K. Residual Stresses—Measurement and Causes in Machining Processes. *CIRP Ann.* **1982**, *31*, 491–510. [CrossRef]
9. Yang, Y.; Li, M.; Li, K.R. Comparison and analysis of main effect elements of machining distortion for aluminum alloy and titanium alloy aircraft monolithic component. *Int. J. Adv. Manuf. Technol.* **2014**, *70*, 1803–1811. [CrossRef]
10. Li, J.; Wang, S. Distortion caused by residual stresses in machining aeronautical aluminum alloy parts: Recent advances. *Int. J. Adv. Manuf. Technol.* **2017**, *89*, 997–1012. [CrossRef]
11. Weber, D. Investigation on the scale effects of initial bulk and machining induced residual stresses of thin walled milled monolithic aluminum workpieces on part distortions: Experiments and finite element prediction model. *Procedia CIRP* **2021**, *102*, 337–342. [CrossRef]
12. Bates, C.E. Selecting quenchants to maximize tensile properties and minimize distortion in aluminum parts. *J. Heat. Treat.* **1987**, *5*, 27–40. [CrossRef]
13. Prime, M.B.; Hill, M.R. Residual stress, stress relief, and inhomogeneity in aluminum plate. *Scr. Mater.* **2002**, *46*, 77–82. [CrossRef]
14. Robinson, J.S.; Tanner, D.A.; Truman, C.E. 50th Anniversary Article: The Origin and Management of Residual Stress in Heat-treatable Aluminium Alloys. *Strain* **2014**, *50*, 185–207. [CrossRef]
15. Sim, W.M. Challenges of residual stress and part distortion in the civil airframe industry. *Int. J. Microstruct. Mater. Prop.* **2010**, *5*, 446. [CrossRef]
16. Barcenas, L.; Ledesma-Orozco, E.; Van-der-Veen, S.; Reveles-Arredondo, F.; Rodríguez-Sánchez, E.A. An optimization of part distortion for a structural aircraft wing rib: An industrial workflow approach. *CIRP J. Manuf. Sci. Technol.* **2020**, *28*, 15–23. [CrossRef]
17. Wang, Z.; Sun, J.; Liu, L.; Wang, R.; Chen, W. An analytical model to predict the machining deformation of frame parts caused by residual stress. *J. Mater. Process Technol.* **2019**, *274*, 116282. [CrossRef]
18. Carlisle, O.J. Modelling the Effects of Residual Stress and Material Removal in Sheet Metal Forming. Ph.D. Thesis, University of Ulster, Coleraine, UK, 2012.
19. Jiang, Z.; Liu, Y.; Li, L.; Shao, W. A novel prediction model for thin plate deflections considering milling residual stresses. *Int. J. Adv. Manuf. Technol.* **2014**, *74*, 37–45. [CrossRef]
20. Fan, L.; Tian, H.; Li, L.; Yang, Y.; Zhou, N.; He, N. Machining Distortion Minimization of Monolithic Aircraft Parts Based on the Energy Principle. *Metals* **2020**, *10*, 1586. [CrossRef]
21. Andersch, C.; Ehlers, M.; Hoffmann, F.; Zoch, H.-W. Systematic analysis of the correlation between part geometry and distortion due to heat treatment. *Mater. Werkst.* **2006**, *37*, 23–28. [CrossRef]
22. Yang, Y.; Li, X.; Li, L.; He, N.; Zhao, G.; Chen, N.; Lan, H.; Zhou, Z. Investigation on deformation of single-sided stringer parts based on fluctuant initial residual stress. *J. Mater. Process Technol.* **2019**, *271*, 623–633. [CrossRef]
23. Schajer, G.S. (Ed.) *Practical Residual Stress Measurement Methods*; Wiley: Chichester, UK, 2013.

24. Guo, J.; Fu, H.; Pan, B.; Kang, R. Recent progress of residual stress measurement methods: A review. *Chin. J. Aeronaut.* **2019**, *34*, 54–78. [CrossRef]

25. Aurrekoetxea, M.; Llanos, I.; Zelaieta, O.; Lopez de Lacalle, L.N. Improving accuracy of bulk residual stress characterization in ribbed geometries through equivalent bending stiffness. *Procedia CIRP* **2021**, *102*, 325–330. [CrossRef]

26. Aurrekoetxea, M.; Llanos, I.; Zelaieta, O.; Lopez de Lacalle, L.N. Towards advanced prediction and control of machining distortion: A comprehensive review. *Int. J. Adv. Manuf. Technol.* **2022**, *122*, 2823–2848. [CrossRef]

27. Timoshenko, J.N.G. *Theory of Plates and Shells*; McGraw-Hill Book Company, Incorporated: New York, NY, USA; London, UK, 1940.

28. Dreier, S.; Denkena, B. Determination of Residual Stresses in Plate Material by Layer Removal with Machine-integrated Measurement. *Procedia CIRP* **2014**, *24*, 103–107. [CrossRef]

29. Aurrekoetxea, M.; López de Lacalle, L.N.; Llanos, I. Machining Stresses and Initial Geometry on Bulk Residual Stresses Characterization by On-Machine Layer Removal. *Materials* **2020**, *13*, 1445. [CrossRef] [PubMed]

30. Aurrekoetxea, M.; Lopez de Lacalle, L.N.; Zelaieta, O.; Llanos, I. Uncertainty assessment for bulk residual stress characterization using Layer Removal method. *Exp. Mech.* **2023**, *63*, 323–335. [CrossRef]

31. *ANSYS@ Mechanical User's Guide*; ANSYS Inc.: Cannon Sburg, PA, USA, 2021.

32. Madariaga, A.; Perez, I.; Arrazola, P.J.; Sanchez, R.; Ruiz, J.J.; Rubio, F.J. Reduction of distortions in large aluminium parts by controlling machining-induced residual stresses. *Int. J. Adv. Manuf. Technol.* **2018**, *97*, 967–978. [CrossRef]

33. *ASTM E837-20*; Standard Test Method for Determining Residual Stresses by the Hole-Drilling Strain-Gage Method, Standard Test Method E837-08. American Society for Testing and Materials: West Conshohocken, PA, USA, 2008.

34. Grant, P.V.; Lord, J.D.; Whitehead, P.S. *The Measurement of Residual Stresses by the Incremental Hole Drilling Technique*; National Physical Laboratory: Middlesex, UK, 2002.

35. Chighizola, C.R.; D'Elia, C.R.; Weber, D.; Kirsch, B.; Aurich, J.C.; Linke, B.S.; Hill, M.R. Intermethod Comparison and Evaluation of Measured Near Surface Residual Stress in Milled Aluminum. *Exp. Mech.* **2021**, *61*, 1309–1322. [CrossRef]